Magnetic Resonance Imaging, Vol. 6, pp. 143–155, 1988
Printed in the USA.

0730-725X/88 $3.00 + .00

● *Original Contribution*

CORRECTION OF SPATIALLY DEPENDENT PHASE SHIFTS FOR PARTIAL FOURIER IMAGING

JAMES R. MACFALL, NORBERT J. PELC, AND ROBERT M. VAVREK
General Electric Medical Systems
Milwaukee, Wisconsin 53201

Partial Fourier MR images (PFI) are constructed from data that have fewer phase encoding views than are conventionally acquired using direct Fourier transform spin echo acquisition. The PFI data acquisition is structured to obtain the same spatial resolution as conventional acquisition, trading off signal-to-noise reduction for acquisition time improvement. The "missing" views can be zero filled or, if the data are Hermitian, supplied by symmetry (basic algorithm). The effect of spatially dependent phase shifts (SDPS) on PFI constructed with zero-fill or the basic algorithm is illustrated. The causes and typical magnitudes of such SDPS are discussed. In spin echo data only the low order, slowly varying SDPS, is shown to be significant. Through use of simulated and actual data sets these typical SDPS are shown to produce significant artifacts in PFI, when the amount of missing data is close to one-half. The artifacts are reduced when less data are missing. Good images can be generated with the zero-fill algorithm if less than 25% of the data is missing. Several methods of correcting phase shifts in PFI are developed: the basic Hermitian algorithm with frequency (x) direction correction (BAX), basic Fourier correction algorithm (BFC) and an improved iterative Fourier correction algorithm (IFC). The BFC and IFC can produce good images when as much as 46% of the data is missing. Data with rapidly varying SDPS, for example, gradient refocused data, make the phase correction task more difficult. With less than 25% of the data missing, however, acceptable gradient refocused PFI images can be created.

INTRODUCTION

The direct Fourier transform (DFT) MR imaging method,[1,2] under the assumption that the imaged object is real, produces data with Hermitian symmetry.[3,4] In this case, only one-half of the usual data needs to be acquired, allowing a scan time reduction of a factor of one-half and the penalty of a signal-to-noise reduction of a factor of $1/\sqrt{2}$. Such images will be referred to here as partial Fourier images (PFI).

In practice, an MR image is, of course, truly complex, even though magnitude images are usually displayed. Spatial domain effects such as flow, rf phase shifts, T_2 decay during the sampling window and B_0 inhomogeneity (in the case of gradient echoes) produce spatially dependent phase shifts (SDPS) that cause the image to have imaginary components and the data to be non-Hermitian.

In the time domain, incorrect cable lengths, misadjusted quadrature signal detection, shifts of the sampling grid such that an acquired spin echo is not centered in the data acquisition window and gradient eddy currents that cause the echo to shift during acquisition also cause the data to be non-Hermitian. While such time domain effects are not strictly SDPS, each can be viewed as being caused by an "equivalent" SDPS. For example, if the spin echo is shifted in the sampling window, it can be viewed as being caused by a linearly varying spatial phase shift via the Fourier frequency shift theorem.[5]

PFI have been previously reported by Feinberg.[6] Also, a number of abstracts have appeared in the conference literature in recent years.[7–9] However, the correction of SDPS in order to create Hermitian data sets for PFI has not been widely treated in the open literature.

RECEIVED 9/4/87; ACCEPTED 10/1/87.
Acknowledgments—The authors wish to thank Dr. G. Glover and Dr. S. Flax for many helpful discussions.
Address correspondence and reprint requests to: James R. MacFall, Applied Science Laboratory, General Electric Medical Systems, P.O. Box 414, W-875, Milwaukee, WI 53201.

In this article the type and magnitude of various SDPS in typical high field (1.5T) MR "spin warp"[2] images are evaluated. The artifacts associated with each type of SDPS are demonstrated using simulated MR data. The ability of various phase shift correction schemes to reduce these artifacts in simulated and actual data is presented. The approach adopted is to correct the SDPS so that a complete data set can be created using Hermitian symmetry which then allows existing two-dimensional Fourier transform MR image reconstruction programs to be used, as opposed to use of MEM[11] or ARMA[10] techniques, which require fundamentally different methods of image reconstruction.

BASIC PFI ALGORITHM

In DFT imaging an $N \times N$ point complex data set, $S(k_x, k_y)$ is collected for:

$$\begin{aligned} k_x &= n\Delta k + k_{ox} \qquad n = 1, \ldots, N \\ k_y &= m\Delta k + k_{oy} \qquad m = 1, \ldots, N \end{aligned} \tag{1}$$

where $\Delta k = 2\pi/D$ and D is the length of one side of the square field-of-view (FOV). Nominally, $k_{oy} = k_{ox} = -(N/2 + 1)\Delta k$. The pulse sequence is repeated for $m = 1, \ldots, N$ and at each repetition the N values of k_x are collected. It is possible to have $M \times N$ data sets where $M \neq N$. Here the case $M = N$ will be treated for simplicity although the extension to the $M \neq N$ case is straightforward. Each such collection at a given k_y can be repeated N_{ex} times and the results averaged to give improved signal-to-noise with consequent lenghtening of the acquisition time. The N data points for a given k_y are referred to as a "view" of data. PFI is useful when $N_{ex} = 1$ and it is desired to further reduce the imaging time. If the image is real, that is, if the data $S(k_x, k_y)$ are Hermitian then:

$$S(-k_x, -k_y) = S^*(k_x, k_y) \tag{2}$$

where "*" indicates complex conjugation. Hence, it is only necessary to gather data for $m \leqq N/2 + 1$. The data for $m = N/2 + 2$ through $m = N$ can be obtained from the symmetry relation Eq. (2). The full data set forms an $N \times N$ complex matrix. An image is constructed by computing the two dimensional Fourier transform of the measured data matrix. This is typically accomplished by computing N one dimensional Fourier transforms (FT) along the rows (k_x direction) and then N one dimensional column FT's (k_y direction).

In the PFI case the data for the rows exist up to $m = N/2 + 1$. Hence the k_x direction transforms can be completed giving $S'(x, k_y)$. The Hermitian symmetry relation is now confined to the k_y direction:

$$S'(x, -k_y) = [S'(x, k_y)]^*. \tag{3}$$

Since the exact center of the data is often difficult to find, this formulation reduces a two dimensional problem as in Eq. (2) to a one dimensional one.

Hence, the basic PFI algorithm as used here consists of (1) acquiring data for $m = 1$ to $N/2 + 1$, (2) computing the k_x direction transforms, (3) applying Eq. (3) to obtain $S'(x, k_y)$ for $m = N/2 + 2$ to N and (4) computing the final k_y direction transforms to get the image.

It is useful to consider a simple example. Let $f(x)$ be a simple complex function whose imaginary part is zero:

$$\begin{aligned} \mathrm{Re}\{f(x)\} &= \begin{cases} A & -L < x < L \\ 0 & \text{elsewhere} \end{cases} \\ \mathrm{Im}\{f(x)\} &= 0 \ . \end{aligned} \tag{4}$$

The FT, $F(k_y)$, of this function is:

$$\begin{aligned} \mathrm{Re}\{F(k_y)\} &= 2AL\sin(Lk_y)/(Lk_y) \\ \mathrm{Im}\{F(k_y)\} &= 0 \ . \end{aligned} \tag{5}$$

Since $f(x)$ is real, the FT of $f(x)$ is Hermitian, i.e.,

$$F(-k_y) = F^*(k_y) \ . \tag{6}$$

The practical translation of this is that the real part of F is symmetric about $k_y = 0$ (even) and the imaginary part is anti-symmetric (odd).[5] In particular, $F(k_y = 0)$ should be equal to zero.

Phase shifts of $f(x)$ will destroy the Hermitian symmetry. Consider $f'(x)$:

$$f'(x) = e^{ip(x)} f(x)$$

and

$$p(x) = s_0 + s_1 x + s_2 x^2 \tag{7}$$

Thus, $f'(x)$ is a (possibly spatially dependent) phase shifted version of $f(x)$. Let $F'(k_y)$ be the FT of $f'(x)$. If s_1 and s_2 are zero then $F'(k_y)$ is just multiplied by a constant phase factor. However, while F' is still symmetric about $k_y = 0$, it is no longer real. Also, $\mathrm{Im}\{F'(k_y = 0)\}$ is not equal to zero. Hence, a

simple constant phase shift can make a function no longer Hermitian. If $s_0 = s_2 = 0$ but $s_1 \neq 0$ then by the frequency shift theorem $F'(k_y) = F(k_y - s_1)$. Now F' is no longer symmetric about $k_y = 0$ and is thus no longer Hermitian. Finally, if $s_2 \neq 0$ then F' is the convolution of F with a function that is symmetric in both the real and imaginary parts. This function thus has a symmetric imaginary part, which makes F' not Hermitian.

Hence, it is easy to see that simple, low order phase shifts of an input function whose FT is Hermitian will produce an output function whose FT is no longer Hermitian, since the modified input function is no longer real.

SPATIALLY DEPENDENT PHASE SHIFTS

Figure 1(a)–(d) shows the magnitude, phase, real and imaginary images for a typical 256 × 256 DFT "spin warp" MR head scan at 1.5T for a 24 cm FOV. The modulation in the real, imaginary and phase images that shows up as bands are mainly due to a linear SDPS generated by the spin echo not reaching its peak at the center of the data acquisition window. For every sampling interval in k_x, k_y that the echo is displaced from the center of the window a 2π cycle of modulation appears in these images. The distinct discontinuities in the phase image are due to the $\pm\pi$ range of the two-argument arctangent function. The intensity scaling of $\pm\pi$ is thus apparent from the image. The pixels outside the object have nearly random values of phase since the arctangent of the ratio of two random variables with zero mean is being computed.

The magnitude and phase along the line AA′ shown in Fig. 1(c) are graphed in Fig. 2. Spatial dimensions such as the y-axis distance as shown here will be given in pixels for convenience. Inside the brain the major trend in the phase is a low order smooth variation. The prominent exceptions are at locations of flow and air-tissue interfaces. A fit of a 5th order polynomial to the phase data:

$$p(y) = a_0 + a_1 y + a_2 y^2 + a_3 y^3 + a_4 y^4 \qquad (8)$$

gives $a_0 = -3.94$, $a_1 = 3.45 \times 10^{-2}$, $a_2 = -8.07 \times 10^{-5}$, $a_3 = 9.32 \times 10^{-8}$ and $a_4 = 1.5 \times 10^{-10}$, where p is given in radians, y in pixels. For the purposes of this fit, data outside the skull and the data causing the sharp phase shift for the flowing blood at the base of the skull were excluded. At $y = 100$ (pixels) the first three terms account for 99.9% of the change from point to point, while the last two only supply 0.1%.

This indicates that the major phase variation terms are the constant, linear and quadratic ones. In the imaging system used, since no particular effort was made to perfectly adjust these phase shifts, the constant phase shift could be anywhere in the range $\pm\pi$. The x direction linear phase shift due to the echo peak not being aligned with the point at $n = N/2 + 1$ amounts to a 2π phase modulation for every full data sample shift of the center of the echo. Typically the echo is centered to within ±3 data samples. In the y

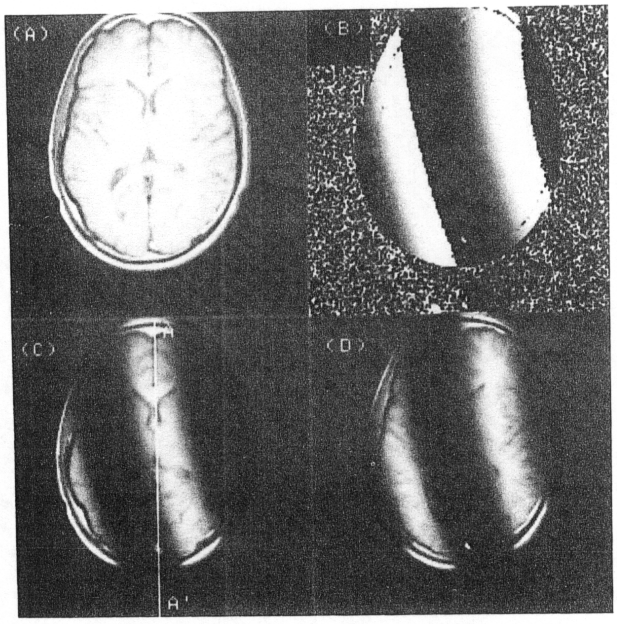

Fig. 1. Typical 256 × 256 DFT MR image: (A) magnitude, (B) phase, (C) real, (D) imaginary.

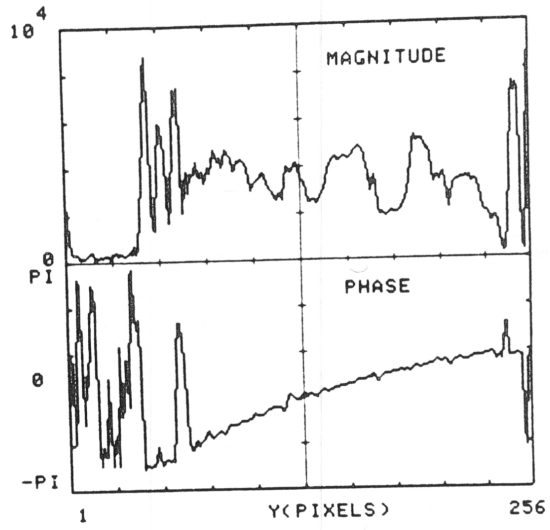

Fig. 2. Graph of magnitude (top) and phase (bottom) along line AA′ shown in Fig. 1(C).

direction the "pseudo-echo" peak not being at $m = N/2 + 1$ will also induce a linear phase shift. The y direction is usually much better controlled in this regard. Typically there is no more than a ± 0.5 sample shift of the y direction "pseudo-echo" peak. This is well illustrated by Fig. 1 in which there are about three cycles of modulation in the x direction, but only one-half a cycle of modulation in the y direction. As a function of x the quadratic term will vary, being larger in the center and smaller at the edges of the object. A value of $s_2 = 0.0001$ was observed to be a reasonable one to use as typical in Eq. (7).

A constant, overall non-zero phase shift can be due to electronic delays that cause the frequency source (local oscillator) and the signal to not be in phase. A linear spatial phase shift can be caused by the data not being centered in the data acquisition window. Quadratic spatial phase shifts are likely due to rf phase shifts because of the conductive nature of the imaged object.

Experience has shown that most spin echo images generated on the MR imager used to obtain Fig. 1 have phase images that are dominated by terms no higher than quadratic. The exceptions, as in Fig. 1, are in regions of flow and motion, which usually are not the dominant effect except, perhaps, some scans of the heart and abdomen. For the purposes of this article, the assumption will be made that the principal phase shifts are of low order, which is typically the case in the head, pelvis and extremities.

It is easy to see the effect of such SDPS on a PFI image by using a subset of the data for Fig. 1. If the first $N/2 + 1$ views ($N = 256$) of the data for Fig. 1 are treated using the basic PFI algorithm, making the assumption that the data are Hermitian about view 129, the image of Fig. 3(a) results. The artifacts that result from the non-Hermiticity of the data due to the SDPS's are evident.

The principal artifacts are obviously due to the x direction linear SDPS that produce the broad bands in Fig. 1. Since the data are complete in the x direction, it is possible to perform a constant and linear x direction phase correction on the data. The correction factors are obtained from the data in the manner outlined in reference 12. Every view, after the x direction FT, is then corrected for linear, constant SDPS using the same correction factors for all views. This avoids inducing any k_y direction phase shifts. This is termed the basic algorithm with x phase correction (BAX algorithm). Figure 3(b) shows the PFI image produced with the BAX algorithm. The image still exhibits some "smearing," but the major banding has been corrected.

Since phase shifts still exist, it may actually be possible to cause worse artifacts by use of Eq. (3). Figure 3(c) is a reconstruction for which no x direction phase correction is performed and Eq. (3) is not used. The data were simply zero filled from $m = 130$ to $m = 256$ before the y direction FT was performed (zero-fill algorithm). While there are no obvious intensity artifacts, the image is smeared along the y direction, with obvious loss of resolution and contrast. The fact that the zero-fill algorithm is an improvement on the BAX algorithm does show, however, that in the presence of phase shifts the use of non-existent symmetry properties can actually create artifacts.

It is possible to create a truly Hermitian data set for the image of Fig. 1(a) by computing the inverse FT of a complex image which has its real part equal to the magnitude image of Fig. 1(a) and which has its imaginary part set to zero. These data are Hermitian about the point $m = 129$ when a 256 point FFT is used. When a PFI image is constructed from the first 129 views of such a data set using the basic algorithm the image is identical to the original magnitude image. Hence the artifacts of Fig. 3(a)–(c) are indeed due to the phase shifts.

A question that naturally occurs is whether correction of constant and linear SDPS in both the x and y directions is sufficient for adequate PFI images. By

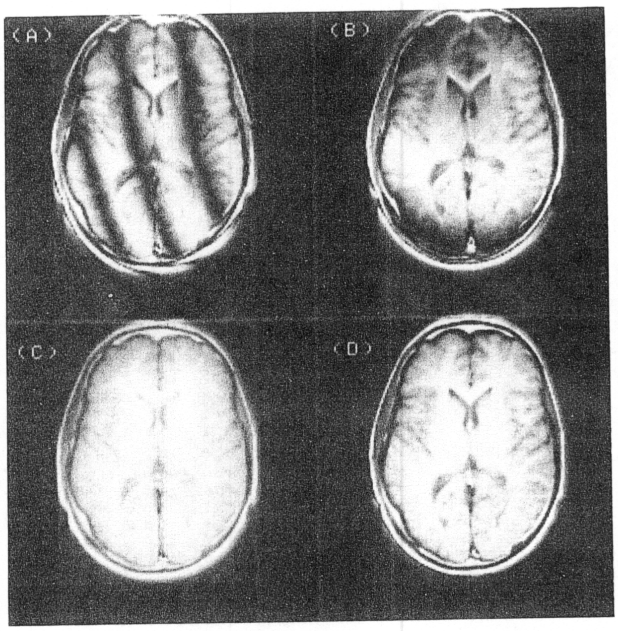

Fig. 3. PFI showing artifacts from various algorithms: (A) basic algorithm, (B) BAX algorithm, (C) zero-fill algorithm, (D) basic algorithm using data that had prior constant, linear SDPS correction, illustrating artifacts from higher order SDPS.

correcting the linear and constant terms in Fig. 1 and then creating a data set by inverse FT, as described above, a data set with only the higher order terms can be created. A PFI image using this data set and the basic algorithm is shown in Fig. 3(d). While it doesn't show any of the banding of Fig. 3(a), and is improved compared to Fig. 3(c), it is still "smeared" or "blurry" indicating that higher order correction is important.

CORRECTION OF SDPS

The central problem of PFI formation, then, is estimation and correction of SDPS for a data set that contains less than the N views required for reconstruction of a full, complex image. An obvious approach is to acquire some extra "overscan" views beyond the $m = N/2 + 1$ view in order to estimate the SDPS. If views from $m = 1$ to $m = N/2 + 1 + m_{ov}$ views are collected then a complex image of the object can be constructed using views $m = N/2 + 2 - m_{ov}$ to $m = N/2 + 1 + m_{ov}$ over the full FOV that has full resolution in the x direction and low resolution in the y. This "image" would be constructed from a complete data set for the resolution obtained and hence would be free from the PFI artifacts shown in Fig. 3 that could bias estimates of the SDPS.

In practice it is not necessary to actually compute the low resolution image. Since the k_x direction data are complete, the k_x direction FT's can be computed leaving a data set in which each column (k_y direction) can be treated independently as in the basic algorithm. Additionally, an x direction constant and linear phase correction is performed as described previously. A major advantage of this column-by-column phase determination and correction is that it allows correction of SDPS that depend both on powers of x,y separately and crossterms like xy (and higher terms) since a different phase correction is allowed for each column. Of course, the maximum power of y involved is determined by the resolution of the estimator "image" in the y direction.

In each column, then, a low resolution estimate of the SDPS is made from the center $2m_{ov}$ data points. The estimate is used to correct the full data from $m = 1$ to $m = N/2 + 1 + m_{ov}$. After this correction the data should be nearly Hermitian. Hence, Eq. (3) can be used to correctly complete the data from $m = N/2 + 2 + m_{ov}$ to $m = N$. The image is then formed by computing the final, k_y direction FT.

The estimate of the SDPS is made by windowing the center $2m_{ov}$ points with an appropriate function such as a Hanning window centered at $m = 129$, "zero filling" on both sides of the data to have N points and then computing an N point FFT of this data. The phase at each point of this FFT data is the phase estimate of the corresponding point in the eventual image. The window function is important for suppression of data truncation artifacts in the FT. Without the window the phase estimate will contain artifacts that will eventually induce artifacts in the final PFI.

A simple approach to actually making the correction is to combine the data from $m = 1$ to $m = N/2 + 1 + m_{ov}$ with zero filling to $m = N$ and compute the N point FFT of the result. Each point in this data is then multiplied by the inverse of the phase estimate for that point. The result is then again transformed back to k-space to be the phase corrected data. Essentially, this performs a "Fourier" interpolation of the data to the phase corrected set of points. K-space (time domain) schemes may be able to perform this correction adequately, but the Fourier one is conceptually simple and easily implemented in an image reconstruction program since a rapid FT is already available.

When the relation Eq. (3) is used on the corrected data, it is useful to discard m_d points near $m = N/2 + 1 + m_{ov}$ since there will be some "Fourier leakage" there if the correction is large. Hence, the points from $m = N/2 + 2 + m_{ov} - m_d$ to $m = N$ are replaced using Eq. (3). The foregoing PFI algorithm will be called the basic Fourier correction algorithm (BFC algorithm).

As an example, suppose the image domain data for a given image line is the rectangular function of Eq. (5) and that it has an SDPS as in Eq. (7). The k-space data for this line would then be the FT of this function. Figure 4(a) shows the magnitude for the center points of the FT of Eq. (5) for $L = 48$ (pixels), $A = 100$ and $N = 256$. The k_y distance is scaled in pixels for convenience. The center point thus occurs at $m = 129$ (the center point for these plots) for a 256 point FFT that has a standard linear phase shift of 1/2 of the FOV applied to keep the "echo" centered. Figure 4(b) shows the magnitude for the FT of Eq. (7) with $s_0 = .1$, $s_1 = -.01$ and $s_2 = .0001$, which are typical values for these coefficients. The data are truncated at $m = 137$ to simulate a PFI data set with $m_{ov} = 8$. Note how the center has been shifted and the Hermitian symmetry distorted, when compared to Fig. 4(a). Figure 4(c) shows the result after the data of Fig. 4(b) have been processed using the BFC algorithm with $m_d = 2$. At this scale Figs. 4(a),(c) are very similar as would be expected if the correction scheme is to be successful. Figure 4(d) shows the magnitude of the difference between the function of Fig. 4(a) and that of Fig. 4(c). The differences, on the order of 2%, are due to inaccuracies in the estimation and to "leakage" at the truncation point from the correction step.

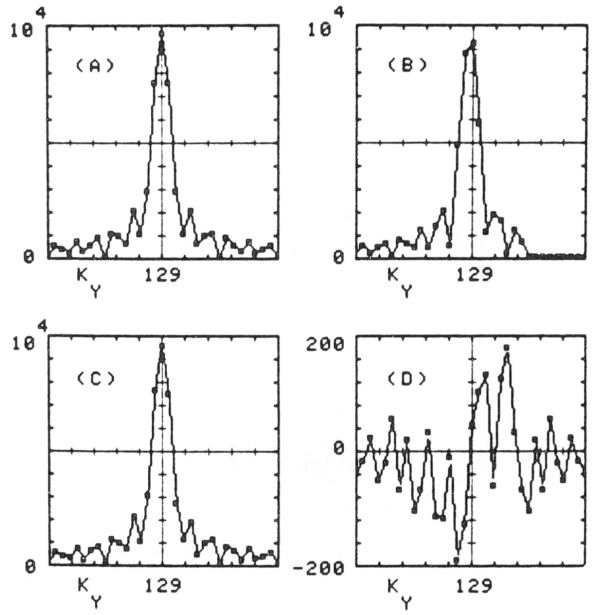

Fig. 4. Graphs showing magnitude of result at various stages of BFC algorithm on 'sinc' function data: (A) sinc with no phase shift, (B) sinc with phase shift, data truncated beyond $m = 137$, simulating PFI data, (C) sinc of (B) after BFC phase estimation and correction, (D) difference of (A) and (C).

One way to answer the question as to whether the BFC algorithm is "good enough" is to see how well full reconstructions agree with PFI images made from subsets of the same data. Figure 5(a) shows a BFC PFI reconstruction performed on the data for the image in Fig. 1 with $m_{ov} = 8$ and $m_d = 2$. Clearly, a good image has resulted. Figure 5(b) shows the difference between Fig. 5(a) and 1(a). The difference image has been scaled to be able to display it with the others. The data in the exterior show noise about zero. The scaling is such that with this window the maximum differences shown (at the edge of the skull) are about 10%. The difference image shows three types of artifacts. The first is some additional streaking from regions of flow. The second is a faint low frequency "ringing" that is consistent with the spatial frequency of $m_{ov} = 8$. Low level artifacts in the exterior have also been generated. The maximum amplitude of these artifacts is less than 5% when compared to the general image amplitude and hence they are not of much consequence. The third artifact is the high frequency "edge map" effect that is most prominent at the top and bottom of the skull. The mismatch at the skull is more prominent in this difference image, but is still a small percent error since the signal there is very large.

Figure 5(c) shows the PFI resulting from a data set with $m_{ov} = 8$ using the BAX algorithm. While the exterior modulation is reduced compared to Fig. 3(b), which had $m_{ov} = 1$, it is not as good as Fig. 5(a).

Figure 6(a) shows the PFI resulting from using $m_{ov} = 8$ with the zero-fill algorithm. When compared to $m_{ov} = 1$, Fig. 3(c), there is some improvement in the exterior, but the interior appears to be the same or somewhat worse. It is not as good as Fig. 5(a) where the more sophisticated BFC algorithm has been used. Figure 6(b) shows the result when $m_{ov} = 64$ is used with the zero-fill algorithm. Figure 6(c) shows the difference image between the complete reconstruction and Fig. 6(b). Scaling similar to that of Fig. 5(b) has been applied for the purpose of display (except that the total offset is slightly different, giving a different overall brightness). For a 50% increase in scan time over the $m_{ov} = 0$ case, this simple technique (3/4 acquisition compared to a full $N = 256$) gives an image nearly as good as the full acquisition technique (but with signal-to-noise intermediate between 1/2 and full acquisition). Evidently, the truncation at higher spatial frequency components (large m_{ov}) does not produce as serious artifacts as truncation of the lower frequencies (small m_{ov}).

SIMULATED SINGLE COMPONENT SDPS

An object which is a square of constant intensity with a different SDPS on each y direction line provides a useful way to visualize how well the various algorithms outlined in the previous sections perform. Figure 7(a) shows the magnitude image of the square (the small square in the upper right-hand corner was included for purposes of orientation). Figure 7(b) shows the phase image for a square in which each column (y direction) has a different constant phase shift ranging from $-\pi$ (left) to π (right). The result is a ramp in phase in the x direction. Figure 7(c) shows the phase image where each column has a different linear phase shift with slope ranging from π/N per pixel to $-\pi/N$ per pixel. Figure 7(d) shows a phase image where each column has a different quadratic phase shift with the quadratic coefficient ranging from $-.0001$ to $.0001$. These values cover the typical ranges noted previously.

Four data sets that produce the images shown in Fig. 7 were calculated from the inverse 2DFT of the complex image whose real and imaginary parts were computed from the magnitude image of Fig. 7(a) and the corresponding phase image. Each data set thus has a range of SDPS of a particular type (none, constant, linear or quadratic). These data sets can then be used to observe the artifacts each particular phase type creates in a final PFI image.

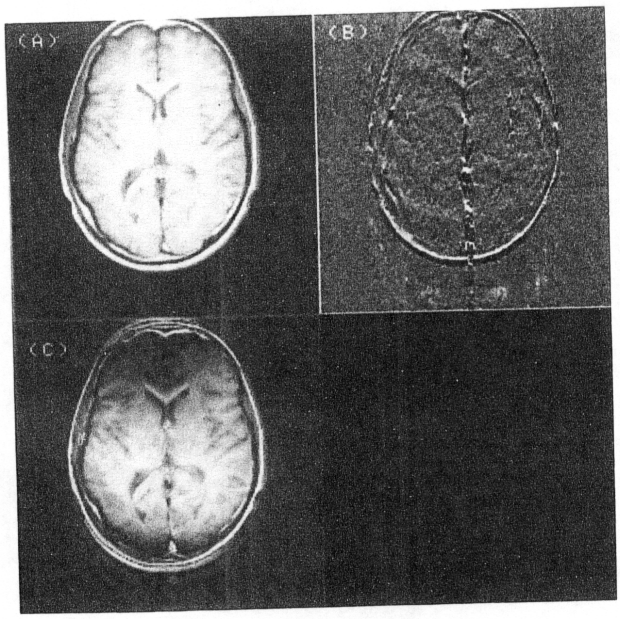

Fig. 5. (A) PFI resulting from the BFC algorithm, $m_{ov} = 8$, $m_d = 2$. (B) difference between magnitude of Fig. 1(A) and 5(A). Difference image is scaled so that maximum brightness is 10% difference. (C) PFI resulting from BAX algorithm with $m_{ov} = 8$.

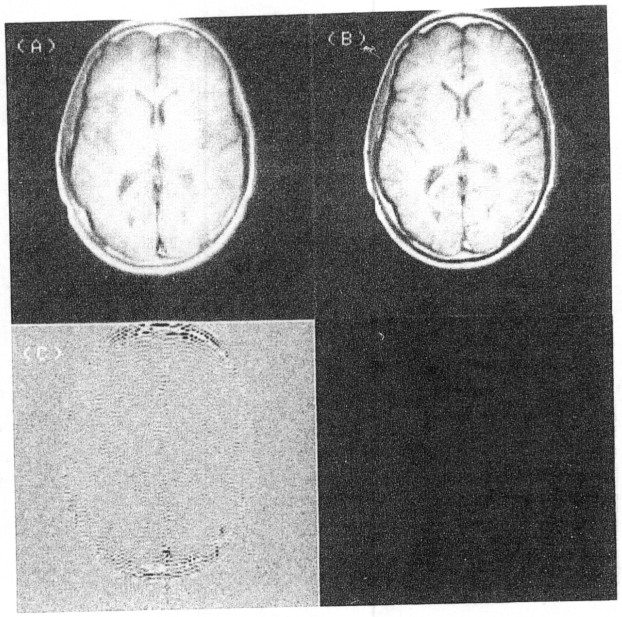

Fig. 6. (A) PFI resulting from the zero-fill algorithm with $m_{ov} = 8$. (B) same as Fig. 6(A) with $m_{ov} = 64$. (C) difference between magnitude of Fig. 6A and 6B, same scaling as in Fig. 5B.

Figure 8 shows the difference between the magnitude image from a full data calculation for each of the data sets and that from a PFI calculation using the basic algorithm with $m_{ov} = 8$. Presumably, a perfect correction will allow a perfect subtraction, thus Fig. 8 shows images of the artifacts generated. The magnitude of the square, as scaled, is 775 hence the window for Fig. 8 is set to about $\pm 2\%$.

Figure 8(a) shows the result for the data set with no phase shifts. In this case the data are Hermitian and the PFI image is as good as the original image, as illustrated by the subtraction image being essentially zero (interior matches the exterior). Figure 8(b) shows the result for the data set with constant y direction phase shifts. The difference image is non-zero everywhere except near the center and edges where the phase is near zero or $\pm\pi$. Figures 8(c) and (d) show the results for the linear and quadratic terms. They exhibit a central region of good reconstruction near where the phase shift is zero. The artifacts get worse as the phase shifts increase away from the center. Also note that the artifacts propogate in the y direction only with large values both inside and outside of the object. It is, of course, no surprise that the basic algorithm is very sensitive to phase shifts. Figure 8 will serve as a baseline to compare the performance of other algorithms.

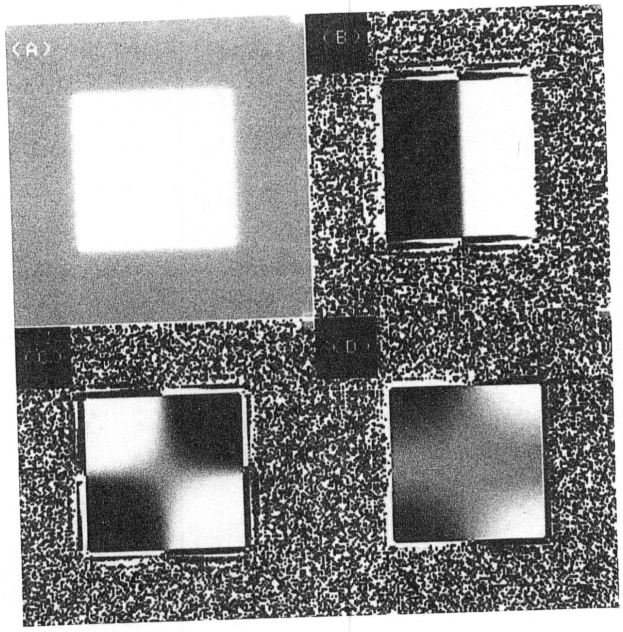

Fig. 7. (A) magnitude image of a square. (B) phase image of square with different constant phase shift for each vertical image line, phase shifts range linearly from -2π on the left to 2π on the right. (C) phase image of square with different linear phase shift for each vertical image line, phase shift factor varies linearly from π/N on the left to $-\pi/N$ on the right. (D) phase image of square with different quadratic phase shift for each vertical image line, phase shift factor varies linearly from $-.0001$ on the left to .0001 on the right.

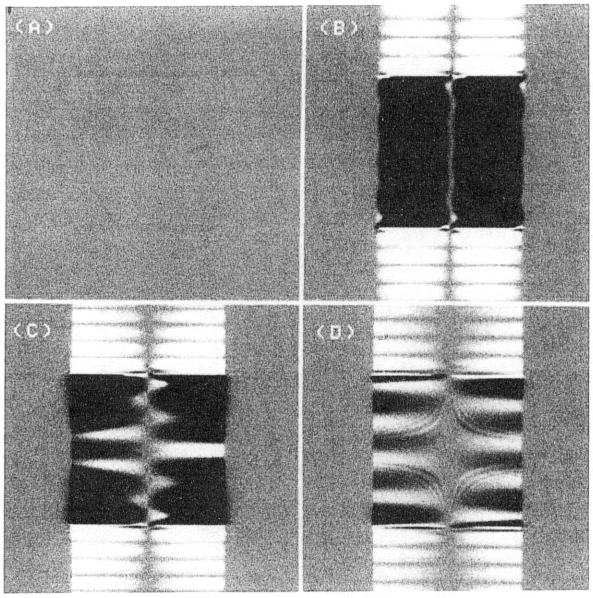

Fig. 8. Images of difference between PFI image made using the basic algorithm and full data image of the square for the various phase shifts: (A) no phase shifts, (B) constant phase shifts, (C) linear phase shifts, (D) quadratic phase shifts.

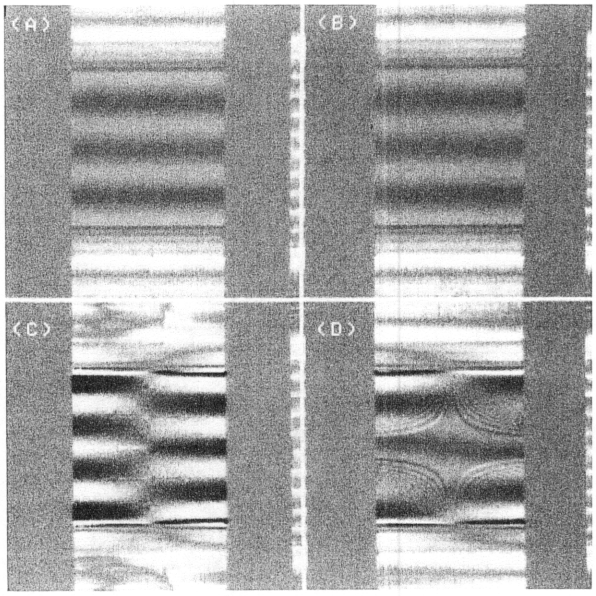

Fig. 9. Images of difference between PFI image made using the BFC algorithm and full data image of the square for the various phase shifts: (A) no phase shifts, (B) constant phase shifts, (C) linear phase shifts, (D) quadratic phase shifts.

A similar set of difference images are shown in Fig. 9 for a PFI that uses the BFC algorithm with $m_{ov} = 8$ and $m_d = 2$. Figure 9(a), for the case of no phase shifts, now shows some small errors. The spatial frequency of the oscillation is consistent with the value of m_{ov}. Hence the BFC technique can induce some small errors into an otherwise Hermitian data set. Figure 9(b) shows the result for constant phase shifts in the y direction. Since these constant phase shifts vary linearly from left to right, they form a phase ramp, which is a linear phase shift in the x direction. The x direction phase shift correction corrects this, giving a result that is similar to Fig. 9(a). Figures 9(c) and (d) show the result for linear and quadratic y-direction phase shifts that vary in the x direction. The artifacts are larger for the larger phase shifts. In the center, where the phase shift is zero, the artifacts are similar to Fig. 9(a). The exterior artifacts have similarly been reduced, but there are a few places with somewhat stronger residual values, that appear at a horizontal line on the top and bottom, midway to the edge of the FOV.

It is clear that the BFC phase correction technique has made a significant reduction of the artifacts that appear in Fig. 8. In Fig. 8 the worst artifacts are due to the constant phase shifts, followed in severity by the linear and then the quadratic. The maximum differences in Fig. 8, in the black regions, approach 100%. The phase correction technique has reduced these artifacts so that the worst remaining ones are due to the linear shifts. The maximum differences are no worse than 10% at the extremes and there are large ranges where the differences are less than 2%.

When a PFI is constructed using the zero fill algorithm, the dominant effect appears to be due to the truncation of the data. Figure 10(b) shows the difference image for the no phase shift square for the zero-fill technique with $m_{ov} = 8$. The spatial frequency of the oscillation is consistent with the choice of m_{ov}. The images for the other types of phase shift are similar to Fig. 10(b). Figure 10(a) shows the same image for the BFC algorithm. The artifacts are much smaller for this technique. As m_{ov} is increased the artifacts become smaller and both techniques begin to give similar results, although the BFC technique is consistently better. Figures 10(c) and (d) show the difference images for the two techniques for $m_{ov} = 64$. The overshoot at the square edge is worse for the zero fill technique (Fig. 10(d)). Note that the oscillation spatial frequency has increased consistently with m_{ov}. The artifacts have decreased mainly due to the fact that there is decreased signal "energy" at the higher spatial frequencies, hence artifacts due to truncation or phase miscorrection at these frequencies will be of lower intensity compared to those generated at lower frequencies.

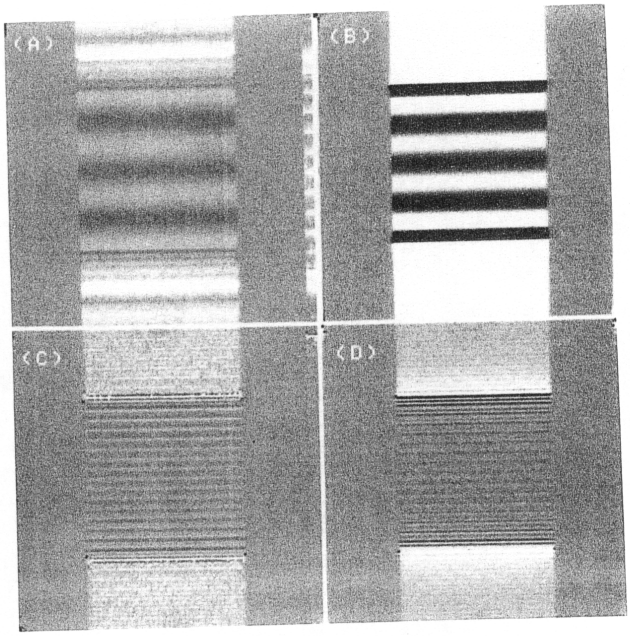

Fig. 10. Images of difference between PFI image made with various algorithms and full data image of the square with the constant phase shift: (A) BFC algorithm, $m_{ov} = 8$, $m_d = 2$, (B) zero-fill algorithm, $m_{ov} = 8$, (C) BFC algorithm, $m_{ov} = 64$, $m_d = 2$, (D) zero-fill algorithm, $m_{ov} = 64$.

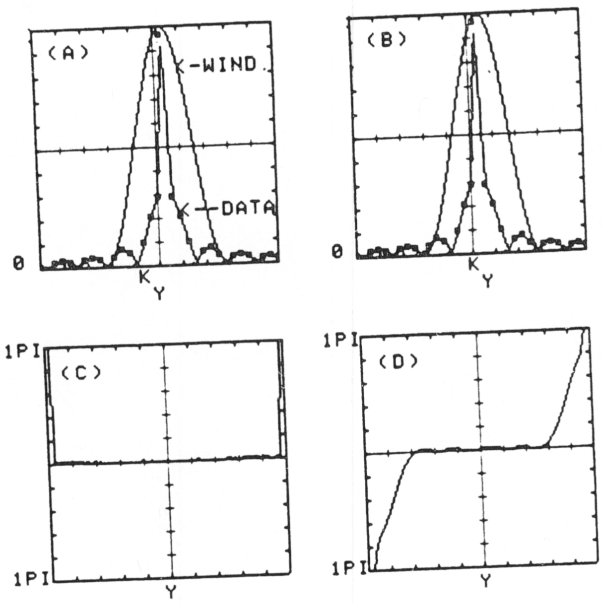

Fig. 11. Graphs showing the effect of window misregistration on phase estimate. (A) window centered on data, (B) window offset by .5 data sample, (C) phase estimate resulting from (A), phase estimate resulting from (B).

Thus the BFC technique performs better than the basic or the zero-fill algorithms for small values of m_{ov} in the presence of typical SDPS. It does have the defect of inducing small artifacts due to use of truncated data in the phase estimation and correction steps.

IMPROVEMENTS TO THE BFC ALGORITHM

There are two sources of error in the BFC algorithm. The first is due to the use of a window function in the phase estimation step and the second is the use of truncated data in the correction step that leads to Fourier "leakage" about the truncation point.

The most serious window effect is due to its centering. Since the data have an unknown phase shift, it is not a priori possible to have the window function centered on the actual peak of the data. Figure 11a shows magnitude of the "raw data," $F(k_y)$, for the center of k-space for a rectangular function as given in Eq. (5) for $A = 100$, $L = 96$ and $N = 256$. The data peak is at point 129 (which is the first point to the right of center on these graphs) since the SDPS is zero. Only the central part of the data, from $m = 113$ to $m = 144$ is displayed. A simple Hanning window function with a width of 16 data points is also shown in Fig. 11(a). If the data are multiplied by this window, zero-filled to $N = 256$ and Fourier transformed, the phase at each point in the transform is zero everywhere inside the rectangle as shown in Fig. 11(c), where the spatial phase is graphed as a function of y from $y = 1$ to $y = 256$ (pixels). The phase at points outside the rectangle was set to a value of $\pi/2$ for the purposes of the figure so that the edge of the rectangle function would be apparent, although the actual value for the phase there is near zero. Hence if the window is centered, the phase estimation gives values close to the correct one (zero) inside the rectangle. Figure 11(b) shows data and a window similar to that of Fig. 11(a) except that the window is shifted by one-half of a data sample. The phase calculated for this window is shown in Fig. 11(d), which is scaled similarly to Fig. 11(c). The miscentered window has systematically lowered the phase estimation on one side of center and raised them on the other side. This creates a nonlinear distortion of the phase estimate that can lead to errors in the phase correction.

The window function can be centered on the data if an estimate of the data center is obtained. The information on the amount that the data are shifted is contained in the linear phase shift term. This may be estimated in a variety of ways such as a weighted average of points or polynomial fitting. Another way is to use the method of reference 12 on the FT of the center $2m_{ov}$ points without windowing. Essentially, this uses a rectangular window (which has minimum

bias for the linear phase shift) on the central points in order to estimate the center of the data.

The data truncation problem can be addressed with an iterative implementation of the BFC algorithm. As it is presented above, the BFC algorithm produces an estimate of a phase corrected, Hermitian data set so that Eq. (3) can be used to complete the data. If these "complete" data then have the SDPS restored, the points in the "data tail" region, from $m = N/2 + m_{ov}$ to $m = N$ become an estimate of the data that would have been acquired for these points. An improved estimate of the complete data set can then be assembled by combining the original data with the estimate of the tail out to $m = N$. The process of phase estimation, correction, use of Eq. (3) and phase restoration can then be repeated on the improved data set to produce a better estimate of the tail. The estimate is improved since on this second iteration the correction step involves the FT of data that includes the improved tail estimate instead of zero-filling as on the first iteration. If a low order spatial frequency estimate of the phase (from the center 2^*m_{ov} points) is sufficient, it only has to be done on the first iteration and then can be used as is for the subsequent ones. In practice it was observed that three iterations produced a strong suppression of the truncation artifact.

The phase restoration step is accomplished in practice by computing the FT of the data after the use of Eq. (3). Since the data are now approximately Hermitian, its phase will be near zero. Hence the phase may be restored by multiplying the FT by a phase factor given by the original phase estimate. The phase restored data are given by the inverse FT. This improved Fourier correction algorithm will be referred to as the IFC algorithm.

Figure 12 shows difference images for the squares with different SDPS created using the IFC algorithm with $m_{ov} = 8$. The oscillatory artifact that is apparent in the no phase shift and constant phase shift cases for the BFC algorithm (Figs. 9(a) and (b)) is now suppressed in the corresponding IFC cases (Figs. 12(a) and (b)). To understand this it is helpful to review the BFC artifact in more detail. In the zero phase shift case, the window is correctly centered and the phase estimation is not affected by incorrect centering. The Fourier transform of a Hanning window, however, does have negative lobes that can cause the estimate of the phase (nominally zero) to give values of π near the edges of the image space. When the truncated data are transformed for phase correction, significant energy corresponding to the truncation exists at the edges of image space where its phase can be (incorrectly) changed by π. This incorrect phase results in

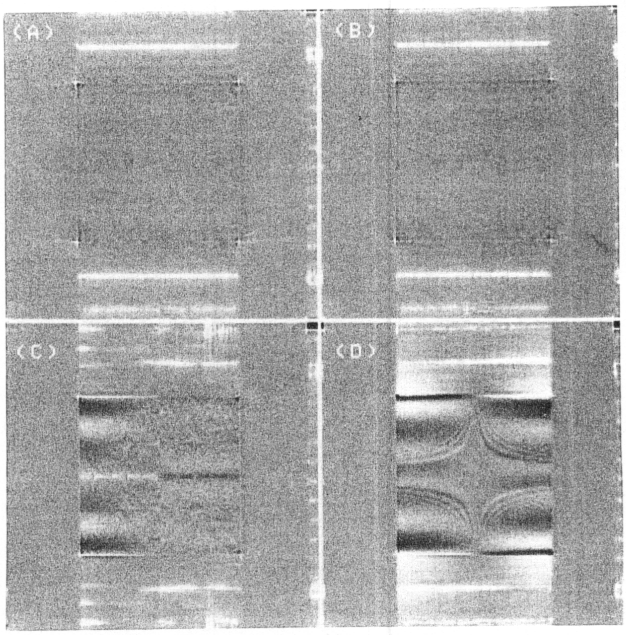

Fig. 12. Images of difference between PFI image made using the IFC algorithm and full data image of the square for the various phase shifts: (A) no phase shifts, (B) constant phase shifts, (C) linear phase shifts, (D) quadratic phase shifts.

the small artifact (at the truncation frequency) in Figs. 9(a) and (b). The IFC algorithm's iterative nature, by supplying a "tail" estimate, reduces the amount of FT energy caused by truncation effects that can have its phase wrongly assigned, hence the artifacts at the truncation frequency are reduced. Different window functions (e.g., those with a positive Fourier transform) may reduce the phase misassignment (for SDPS near zero), but with only a few points in the estimate, the data are always effectively truncated, leading to similar effects.

In the linear phase shift case (Fig. 12(c)) the artifacts have also been significantly improved. The reason for the residual effects at large positive linear phase shifts (on the left-hand side of Fig. 12(c)) is that the data have been shifted sufficiently to cause the central $2m_{ov}$ points to asymmetrically sample the peak region, effectively giving a bias in the phase shift estimation. The quadratic phase shift image, however, shows only slight improvement.

A PFI image using the IFC algorithm on the data of Fig. 1 shows little improvement, since the BFC case is quite good (Fig. 5(a)). Presumably, the SDPS for the data of Fig. 1 are small. Figures 13(a) and (b) show difference images for the PFI created using the BFC and the IFC at a 2% window. Clearly, the IFC

algorithm (Fig. 13(b)) has reduced the artifacts. Figures 13(c) and (d) are PFI for the two algorithms for a uniform water phantom (30 cm dia) in a 48-cm FOV with larger SDPS at a 1% window. The improvement of the IFC (Fig. 13(d)) is evident.

The remaining artifacts are due to secondary effects of the window during the phase estimation step. Just as the information about the size of the linear phase shifts is contained in the position of the peak of the data, the information about the size of the quadratic phase shifts is contained in the width of the central peak area. The window function modifies the width of the central peak, hence biasing the estimate of higher order phase shifts. Using a biased estimate is not as serious, however, as leaving uncorrected the original higher order phase shifts as can be seen from comparing Figs. 12(d) and 9(d) with Fig. 8(d).

While the IFC algorithm is an improvement on the BFC one, its implementation does entail significant extra computation. In clinical images the improvements are barely noticeable when mixed with the structure of the object, even though the object exterior artifacts are reduced. Hence the extra computational burden of the IFC algorithm may not be warranted.

RAPID SDPS VARIATION

When the SDPS vary rapidly in either space or time, one might expect PFI phase correction to fail. Figure 14(a) shows the magnitude of a DFT spin echo image obtained in the pelvis. These data were acquired without cardiac gating or flow moment compensation. Hence there are well known artifacts in the magnitude image due to inconsistent phases of the flowing blood in the femoral arteries. A PFI image made using the data of Fig. 14(a) and the BFC algorithm with $m_{ov} = 8$ and $m_d = 2$ is shown in Fig. 14(b). The two images have a similar appearance with the PFI image also having flow related artifacts. The difference image is shown in Fig. 14(c). The image is scaled to allow display with the others. The low frequency variations in the muscle tissue are on the order of 10% of the muscle intensity. This shows that for stationary tissue the two images are nearly the same but that the flow artifacts are different. Notice, however, that while the artifacts are different in detail, they are actually qualitatively the same. Hence the PFI works reasonably well in this situation.

The reason for the differences, of course, is that the phase estimation is done with low resolution that cannot adequately sample the phase shifts of the small

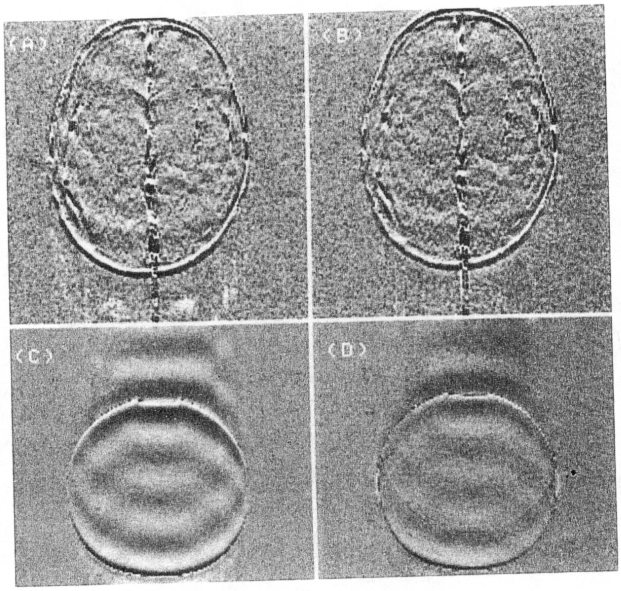

Fig. 13. Images of difference between PFI image made using the BFC or the IFC algorithm and the full data image for a head or a water phantom: (A) head data of Fig. 1(A), BFC algorithm, $m_{ov} = 8$, $m_d = 2$, (B) head data of Fig. 1(A), IFC algorithm, $m_{ov} = 8$, (C) water phantom, BFC algorithm, $m_{ov} = 8$, $m_d = 2$, (D) water phantom, IFC algorithm, $m_{ov} = 8$.

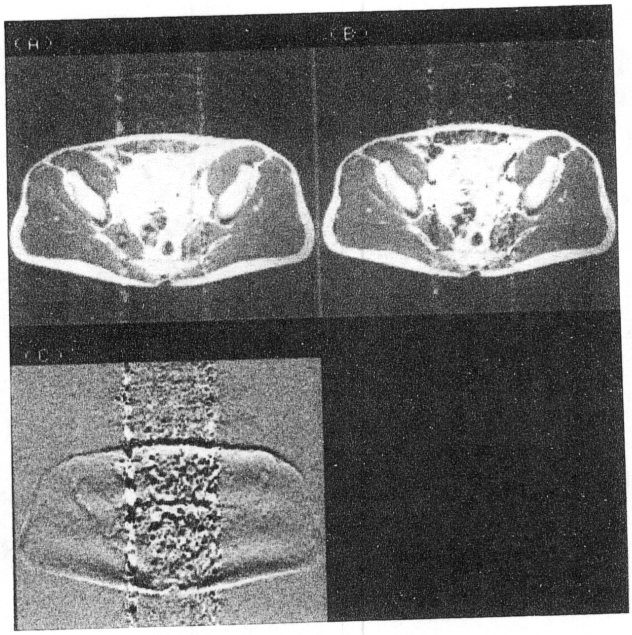

Fig. 14. (A) Full data 256 × 256 DFT spin echo image of a pelvis acquired with no flow or motion compensation. (B) PFI image using the data of Fig. 14(A) and the BFC algorithm with $m_{ov} = 8$, $m_d = 2$. (C) difference image between Fig. 14(A), (B), scaled as in Fig. 5(B).

vessels. In addition there are temporal variations in the phase of the blood. The phase estimation techniques presented here implicitly assume that the phase shifts are constant during the data acquisition. Since the flow artifacts originate from small regions of space, they do not significantly affect the estimate of the low order phase shifts, thus the correction techniques perform adequately for spin echo images where the low order SDPS are the dominant effect. The fact that the flow artifacts are different in detail is reasonable since the data for the image were acquired over a shorter time span for the PFI, giving a different set of flow phase shifts from the full data.

Eddy currents on the readout or phase encoding axis are time dependent effects that could induce equivalent SDPS of higher order. While such effects cannot be ruled out in the data used for the images in this report, the imager used to obtain the data employed hardware measures to minimize eddy current formation through gradient pulse shaping.

Gradient refocused data also contain phase shifts that are not of the low order treated here. The phases of various organs and regions may differ widely depending on the local magnetic susceptibility and/or the B_0 homogeneity. Figures 15(a) and (b) show the magnitude and phase of a gradient refocused image acquired in the pelvis. There are rapid variations of the phase due to organ dependent susceptibility changes as well as inconsistent phase due to flow and motion. Figure 15(c) is the PFI made using a subset of the data of Fig. 15(a) with the BFC algorithm and $m_{ov} = 8$ and $m_d = 2$. The SDPS vary too rapidly for this algorithm to give a good image. The IFC produces little improvement. As m_{ov} increases, however, the image quality improves. Figure 15(d) shows a PFI with $m_{ov} = 64$, $m_d = 2$. Now the image quality appears as good as the full data image. Essentially the larger value of m_{ov} now gives enough information to characterize these SDPS.

Also, as in the spin echo case, with this large value of m_{ov} (1/4 of the full data, corresponding to a 3/4 data acquisition), a PFI made from the data of Fig. 15(a) using the zero-fill algorithm produces an image that is as good as the BFC,IFC image. While the reason for this is not obvious, it may indicate that the artifacts produced by "one-sided" truncation of the data at this value of m_{ov} are reduced below the typical object structure and/or noise level.

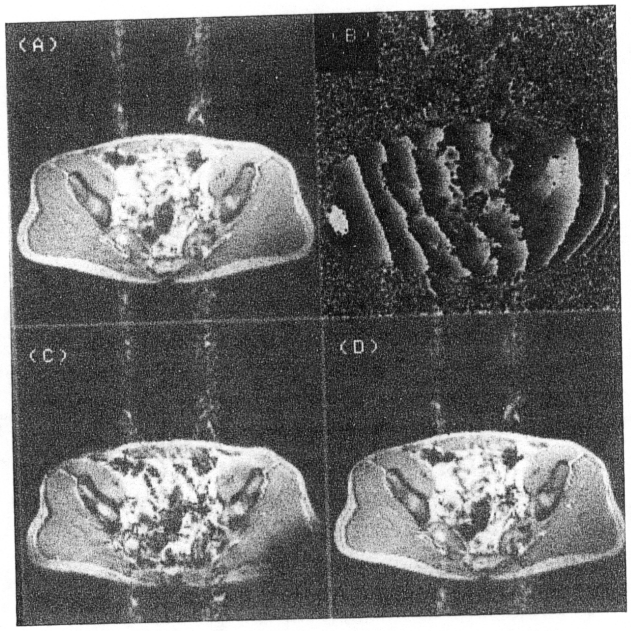

Fig. 15. (A) Full data 256 × 256 DFT gradient refocused echo image of a pelvis acquired with no flow or motion compensation. (B) phase image for Fig. 15(A). (C) PFI image from the data of Fig. 15(A) using the BFC algorithm and $m_{ov} = 8$, $m_d = 2$. (D) same as Fig. 15(C) with $m_{ov} = 64$, $m_d = 2$.

CONCLUSION

The SDPS of spin echo DFT data are primarily of low spatial frequency content. The most important terms are the constant, linear and quadratic ones. In one imaging system the constant phase shifts were found to be principally due to differences in phase between the frequency source and the detected signal as a result of electronic delays. The linear shift was found to be due to the spin echo not forming precisely at the center of the data acquisition window due to gradient offsets. The quadratic term was principally due to phase shift of the rf energy as a result of the conductive nature of the imaged object. No SDPS that were clearly attributable to gradient eddy currents were observed, probably due to careful electronic compensation of the gradient amplifiers (up to 5th order). While one would expect that the constant phase shift could be anywhere in the $\pm\pi$ range, the x,y linear phase shifts should be able to be better constrained by pulse sequence timing adjustment to be less than $\pm 6\pi$ over the FOV. The quadratic term coefficient was observed to be less than ± 0.0001, but this will depend on field strength, object conductivity and rf coil design.

PFI images formed from data with such phase shifts show objectionable artifacts that can appear as bands or smearing in the x or y direction. Constant, linear phase correction of the data in the x direction confines the remaining artifacts to the y direction. These remaining artifacts typically are a subtle smear-

ing or apparent loss of resolution in the y direction. Correction of only the x,y direction constant and linear phase shifts was found to not be sufficient to produce artifact free PFI. When data beyond $m = N/2 + 1$ are acquired and included in the PFI the remaining artifacts usually include a component with a spatial frequency near that of the data truncation frequency.

The PFI algorithms discussed here include the basic algorithm, which is simply an invocation of Hemitian symmetry, the BAX algorithm, which adds a straightforward x direction constant, linear phase correction, the zero-fill algorithm, which doesn't invoke Hermitian symmetry and the BFC,IFC algorithms, which attempt to correct the y-direction phase shifts to various degrees. For small values of m_{ov}, with typical SDPS only the BFC,IFC algorithms perform satisfactorily for spin echo data. The BFC algorithm produces subtle artifacts due to data truncation and biases in the phase estimate from the window function. The IFC algorithm reduces these artifacts but leaves higher order phase estimation bias. The extra computational effort of the iterative IFC algorithm does not seem to warrant its use for the slight improvements it makes. For large values of m_{ov} (e.g., 3/4 data acquisition) the zero fill algorithm, which is computationally simpler, also gives adequate results.

The algorithms presented here implicitly assume that the SDPS are of low spatial frequency and temporally invariant. Data that are acquired of moving objects or with gradient refocused echoes will produce images with phase shifts that violate these assumptions. As long as the motion is confined to small regions, as in blood flow, the artifacts in the PFI images seem to be of the same character, although different in detail, when compared to the full data images. Adequate PFI images can be generated under these conditions if large values of m_{ov} are used. For $m_{ov} = 64$ (3/4 of full data acquisition) good PFI images can be produced in many cases using either the BCF or the simpler zero-fill algorithm.

REFERENCES

1. Kumar, A.; Welti, D.; Ernst, R. NMR Fourier Zeugmatography. *J. Mag. Res.* 18:69–83; 1983.
2. Edelstein, W.; Hutchinson, J.; Johnson, G.; Redpath, T. Spin Warp NMR Imaging and Applications to Human Whole Body Imaging. *Phys. in Med. and Biol.* 25:751–756; 1980.
3. Song, R.; Cho, Z.; Hilal, S. Direct Fourier Transform NMR Tomography with Modified Kumar-Welti-Ernst (MKWE) Method. *IEEE Trans. on Nucl. Sci.* NS-29(1); 1982.
4. King, K.; Moran, P. A Unified Description of NMR Imaging, Data Collection Strategies and Reconstruction. *Med. Phys.* 11(1); 1984.
5. Brigham, E. The Fast Fourier Transform. New York, Prentice Hall, 1974.
6. Feinberg, D.; Hale, J.; Watts, J., Kaufman, L.; Mark, A. Halving MR Imaging Time by Conjugation: Demonstration at 3.5 kG. *Radiology* 161:527–531; 1986.
7. Margosian, P. Faster MR Imaging—Imaging with Half the Data. SMRM Conference Abstracts: 1024; 1985.
8. DeMeester, G.; Patrick, J. Phase Corrections for a Reconstruction Method Using Data Reflection. SMRM Conference Abstracts: 267; 1986.
9. Cuppen, J.; van Est, A. Reduced MR Imaging Time by One-Sided Reconstruction. Topical Conference on Fast MRI Techniques, AAPM and Case Western Reserve; 1987.
10. Smith, M.; Nichols, S.; Henkelman, R.; Wood, M. Application of ARMA Parametric Moving Average Modeling in MRI Reconstruction. *IEEE Trans. on Med. Imaging* 6(3): 132–139; 1986.
11. Gibson, C. MRI Reconstruction by the Maximum Entropy Method. SMRI Conference Abstracts: 83; 1986.
12. Ahn, C.; Nalcioglu, O.; Cho, Z. A New Phase Correction Method in NMR Imaging. SMRM Conference Abstracts: 1446; 1986.